TRANSIENT CHAOTIC DISTRIBUTIONS IN DISSIPATIVE SYSTEMS

by

Kwok Yeung Tsang and M. A. Lieberman

Memorandum No. UCB/ERL M85/56

12 July 1985

ELECTRONICS RESEARCH LABORATORY

College of Engineering
University of California, Berkeley
94720

TRANSIENT CHAOTIC DISTRIBUTIONS IN DISSIPATIVE SYSTEMS

Kwok Yeung TSANG and M. A. LIEBERMAN

Department of Electrical Engineering and Computer Sciences
and the Electronics Research Laboratory
University of California, Berkeley, California 94720

When near-integrable Hamiltonian systems are perturbed by weak dissipation, all persistent chaotic motion is destroyed. However, transiently chaotic motion appears before the trajectories enter embedded islands and are attracted into sinks. We determine analytically such properties as the exponential decay rate of the chaotic transient, the quasistatic distribution for the transiently chaotic region of phase space, and the distribution of trajectories into the various sinks. The dissipative Fermi map is used as an illustrative example.

I. Introduction

Near-integrable, measure-preserving maps are used to model conservative physical phenomena in such fields as celestial mechanics, cosmic ray physics, accelerator theory, and plasma heating and confinement [1]. Conservative systems of nonlinear coupled oscillators are also widely used as physical models. These systems also generate such maps as the phase space orbit repeatedly pierces a Poincaré surface of section.

The phase plane structure in two-dimensional near-integrable measure-preserving maps is well known [2]. There is persistent regular motion on some perturbed KAM orbits and on KAM island orbits surrounding stable fixed points of the map. Regions of persistent chaotic motion are densely interwoven with these regular regions. The measures of the regular and the chaotic regions can vary widely, both within the phase plane and as a function of the system parameters.

New phenomena appear for dissipative systems. Since the (two-dimensional) area of the Poincaré surface of section contracts (by the Jacobian factor J of the map) after each iteration, the motion ultimately lies on a set of lower dimensionality called an attractor. For large dissipation ($J \ll 1$), it is known that one or more strange attractors [3–6] having fractional dimensionality can exist. The persistent motion on a strange attractor is mixing and chaotic. An example is the Hénon [7] attractor. The Hénon map

$$x_{n+1} = y_n + 1 - ax_n^2 \tag{1a}$$

$$y_{n+1} = bx_n \tag{1b}$$

is the most general quadratic mapping with constant Jacobian (= b). For certain values of parameters, say, $a = 1.4$ and $b = 0.3$, the existence of a strange attractor is strongly suggested by numerical iteration.

It is natural to ask whether persistent chaos continuously exists when a Hamiltonian system is smoothly transformed into a strongly dissipative system. The numerical evidence that we present strongly suggests that this does not occur. Instead, an intervening regime of weak dissipation ($1 - J \ll 1$) appears for which all persistent chaotic motion is destroyed. Although the motion may be transiently chaotic over hundreds of thousands of iterations, ultimately the trajecctory is attracted to an embedded island sink and the motion becomes periodic.

To illustrate these features numerically, We consider a modified Hénon map, introduced by Huberman [8], which is (1) with x and y taken modulo 4, i. e.,

$$x_{n+1} = y_n + 1 - ax_n^2, \tag{2a}$$

$$y_{n+1} = bx_n, \tag{2b}$$

$$|x|, |y| \leq 2. \tag{2c}$$

Figure 1a shows the first 10000 iterations of (2) for $a = 1.4$ and $b = 0.9$ with initial condition at $(-0.672, -0.392)$. The y–x plane has been partitioned into 100×100 cells, and the number inside each cell (not readily seen) is a logarithmic measure of the number of occupations, with a blank denoting zero occupations. Bending and folding structures like those in a strange attractor are

seen. Previous work [9,10] introduced an analytical method to obtain invariant distributions f on a strange attractor. Application of this method with $f^{(0)}$ being uniform [9] in the range (2c) yields successive approximations $f^{(0)}, f^{(1)}, \ldots$ to the numerically calculated structures as shown in Fig. 1b–d. It is evident that Fig. 1b–d exhibits structures resembling Fig. 1a. More and more "white" regions are added as the order is increased. Patterns in $f^{(5)}$ look almost identical to those obtained numerically. However, we find numerically that Fig. 1a is an example of transient chaos instead of a strange attractor! Figure 2 shows the trajectories from two different initial conditions chosen at random. These trajectories are attracted to a period six attractor after about 25 000 and 5 000 iterations respectively. It is also found that continual iteration of the trajectory in Fig. 1a yields the same periodic attractor after about 320 000 iterations. We see the existence of transient chaotic motion before the trajectories enter embedded islands and are eventually attracted into sinks.

In the following sections, we present an analytical study of transient chaotic motion for a class of near-integrable Hamiltonian twist maps [2] that are perturbed by small dissipation. We determine analytically such properties as the exponential decay rate of the chaotic transient, the quasistatic distribution for the transiently chaotic region, and the distribution of trajectories into the various sinks.

II. Weakly Dissipative Fermi Map

We illustrate the calculation procedure for transient chaos and compare the results to those obtained by numerical iteration, using as an example the dissipative Fermi map [9,10]. However the procedure is directly applicable when dissipation is introduced into other twist maps such as the Chirikov–Taylor [11,12] and the separatrix maps [2,11]. The Fermi map describes a cosmic ray acceleration mechanism [13] in which charged particles are accelerated by collisions with moving magnetic field structures. In the model, a ball bounces in one-dimensional motion between a fixed and an oscillating wall. We adapt a simplified model [14] in which the moving wall oscillates sinusoidally, $x_\omega(t) = a\cos\omega t$, and elastically imparts momentum to the ball according to its velocity $\dot{x}_\omega$ without the wall changing its position in space. We introduce dissipation by assuming that the ball suffers a fractional loss δ in velocity upon collision with the fixed wall. The map is then

$$\bar{u} = (1-\delta)u_n - \sin\psi_n, \tag{3a}$$

$$\bar{\psi} = \psi_n + 2\pi M/\bar{u}, \tag{3b}$$

$$(\psi_{n+1}, u_{n+1}) = (\bar{\psi}, \bar{u})\,\mathrm{sgn}\,\bar{u}, \tag{3c}$$

where $u_n = v_n/(2\omega a)$ is the normalized ball velocity and $\psi_n = \omega t_n$ is the phase of the oscillating wall, and $M = l/(2\pi a)$ is the normalized distance between the two walls. The function $\mathrm{sgn}\,\bar{u} = \pm 1$ for $\bar{u} \gtrless 0$, and is introduced to maintain $u_{n+1} \geq 0$ for low velocities $u_n < (1-\delta)^{-1}$, as physically occurs in the exact model, while preserving the continuity of the map near $u = 0$. The Jacobian of the map is $1-\delta$, and thus the map is area-preserving for $\delta = 0$.

The primary fixed points of the map are found by setting $u_{n+1} = u_n$ and $\psi_{n+1} = \psi_n (\mathrm{mod} 2\pi)$ in (3). We obtain

$$(u_k, \psi_k) = (M/k, \sin^{-1}(-u_k \delta)), \tag{4}$$

where k is an integer. There are two fixed points for each k : $\psi_k \approx 0$ or $\psi_k \approx \pi$ for $u_k \delta \ll 1$. $\psi_k \approx \pi$ is stable for $u_k > u_s = (\pi M/2)^{1/2}$; $\psi_k \approx 0$ is always unstable. For $\delta = 0$, invariant (KAM) island orbits surround the stable fixed points. The location, stability and bifurcations of these fixed points have been described previously [2,14–17].

We summarize the behavior of the motion, determined by numerical iteration, as the parameters M and δ are varied. For $\delta = 0$, there is no dissipation and the usual Hamiltonian chaos ensues, with intermingled areas of persistent chaotic and regular motion in the (u–ψ) phase plane. Numerical iterations for $10 \lesssim M \lesssim 10^4$ show [14– 17] that the phase plane divides into three characteristic regions: (i) For large velocities, $u \geq u_b \approx 2u_s$, invariant (KAM) curves span the plane in ψ and isolate the narrow layers of stochasticity near the separatrices surrounding the fixed points of the map; (ii) there is an interconnected stochastic region for intermediate velocities, $u_b > u > u_s$, in which invariant islands near stable fixed points of the map are embedded in a stochastic sea; and (iii) there is a predominantly stochastic region for small velocities, $u < u_s$, in which all primary fixed points are unstable. The globally stochastic motion within the connected regions (ii) and (iii) is isolated from region (i) by a KAM barrier at u_b, and has a constant equilibrium invariant distribution $f_0(u, \psi)$ [18].

For weak dissipation, $0 < \delta < \delta_c$, where δ_c depends on M, the numerical iterations show that the fixed points of the Hamiltonian map become attracting centers (sinks), the KAM curves no longer exist, and all persistent chaotic motion is destroyed. An initial phase point chosen randomly in region (iii) then undergoes transient chaotic motion for a mean number of iterations $\bar{N} = \bar{N}(M, \delta)$ before it enters an embedded island in region (ii) and becomes trapped in an island sink. [We also find that when $\delta > \delta_c$ (roughly when δM is large, say, larger than two), then none of one hundred initial phase points entered any island after 5×10^4 iterations. This indicates the possibility of a strange attractor, or at least a very long transient chaos. Studies of the equilibrium invariant distribution for this case were performed in references 9 and 10.]

For the case of transient chaos, Fig. 3 shows the number of unattracted trajectories out of 100 as a function of the number of iterations. After a short transient, we observe that the number decays exponentially for each set of M and δ in Fig. 3. Thus a constant fraction of the remaining trajectories are lost at each iteration.

In Fig. 4, we plot (solid curve) the cumulative phase-integrated distribution

$$\bar{f}(u) = 100 \int_0^N dn \int_0^{2\pi} d\psi f(u, \psi, n)$$

for various M and δ, after $N = 5 \times 10^4$ iterations, for 100 initial conditions at low velocities chosen randomly. We see evidence of attracting sinks between u_s and u_b (except the case $M = 300$ and $\delta = 0.01$, which indicates the existence of a strange attractor, or at least a very long transient chaos). The density leaving the stochastic region flows into these sinks, forming the spikes in the

figure. For all cases studied, the location and structure of these sinks correspond to the Hamiltonian ($\delta = 0$) structure of the stable fixed points (2) of the Fermi map. Sinks of higher periods correspond to secondary fixed points encircling the period one primary fixed points.

An important feature of the numerical results for $\delta \ll 1$ is that an exponentially decaying *quasistatic* distribution

$$f(u, \psi, n) = f_Q(u) \exp(-\bar{\alpha} n) \tag{5}$$

is formed for values of u outside of the "sticky" islands, for $n \gtrsim u_b^2 \approx 2\pi M$. Here, $\bar{\alpha} = \bar{N}^{-1}$ is the exponential rate of decay of the chaotic trajectories. The numerically determined decay rates are given in Table I (first entry). For various M and δ, Table II shows the distribution of trajectories into sinks of period p at $u \approx M/k$ after $N = 50\,000$ iterations (unless otherwise stated) for 100 initial conditions chosen randomly with small u's.

III. Quasistatic Distribution

We now show that the distribution f_Q can be found analytically by solving the appropriate Fokker–Planck equation for the map [19]

$$\frac{\partial f}{\partial n} = \frac{1}{2} \frac{\partial}{\partial u} \left(D \frac{\partial f}{\partial u} \right) - \frac{\partial (Bf)}{\partial u} \approx 0 \tag{6}$$

where, to first order in δ, D is the diffusion coefficient for the area-preserving ($\delta = 0$) map, and $B = -u\delta$ is the friction coefficient due to the dissipation [18]. For $u \lesssim u_s$, $D = 1/2$, the quasilinear value. However, the domain of interest includes the region $u_s \lesssim u \lesssim u_b$, in which the quasilinear diffusion coefficient is

invalid. To obtain an estimate of D in this region, we locally expand (3) in u about a fixed point u_k, which yields

$$I_{n+1} = I_n(1-\delta) + K\sin\theta_n - u_k\delta, \tag{7a}$$

$$\theta_{n+1} = \theta_n + I_{n+1}, \tag{7b}$$

where

$$I_n = -K(u_n - u_k), \tag{8a}$$

$$\theta_n = \psi_n, \tag{8b}$$

and

$$K = 2\pi M/u_k^2 \tag{9}$$

is the stochasticity parameter. For $\delta = 0$, (7) is the Chirikov–Taylor or standard map [20], which has a diffusion coefficient $\bar{D}$ that depends on K. For $K \gtrsim 4$, corresponding to $u \lesssim u_s$, $\bar{D} \approx K^2/2$, the quasilinear value. For $4 \gtrsim K \geq 1$, corresponding to $u_s \lesssim u \lesssim u_b$, one finds

$$\bar{D} \propto (K-1)^\gamma, \tag{10}$$

with the estimate [11] $\gamma \approx 2.5$ for $4 \gtrsim K > 1$ obtained numerically, and the asymptotic result [21,22] near $K = 1$, $\gamma \approx 3.01$. However, over the entire $K > 1$ range, a reasonable fit to the numerical data for $\bar{D}$ is

$$\bar{D} \approx \frac{K^2}{2}\left(\frac{K-1}{K}\right)^\gamma, \tag{11}$$

with $\gamma = 2$. Figure 5 shows the fit of this $\bar{D}$ to the numerically determined data by Murray *et al.* [22]

Transforming from I back to u, we have $D = \bar{D}/K^2$, and using (9) and (11), we obtain, for $u < u_b$,

$$D = \frac{1}{2}(1 - \frac{u^2}{u_b^2})^2. \tag{12}$$

Using $B = -u\delta$ and (12) in (6) and the condition that the net flux is approximately zero, we obtain

$$f_Q(u) = F \exp[-2\delta u_b^2 u^2/(u_b^2 - u^2)], \tag{13a}$$

where

$$F = (2\pi\delta u_b^3)^{-1}[K_1(\beta) - K_0(\beta)]^{-1} \exp(-\beta), \tag{13b}$$

$\beta = u_b^2\delta$, K_1 and K_0 are the modified Bessel functions, and

$$2\pi \int_0^{u_b} du f_Q(u) = 1.$$

This distribution, scaled to the value of $\bar{f}$ at $u = 0$, is plotted as the dashed line in Fig. 4 for the various sets of M and δ. The agreement with the numerical result outside the island regions is generally good.

We can also try to use $\gamma = 3$ to obtain f_Q. We find that for $\delta M \gtrsim 1$, f_Q obtained for $\gamma = 2$ is very close to that for $\gamma = 3$. However, for $\delta M \lesssim 0.3$, $\gamma = 2$ yields a better f_Q to approximate $\bar{f}$ for most values of u. The difference between $\gamma = 2$ and $\gamma = 3$ is shown in Fig. 4, where the $\gamma = 3$ result is plotted as the dotted line.

IV. Exponential Decay Rate

As mentioned before, we see secondary island chain sinks surrounding the primary island sinks. This phenomenon can be understood by again looking at (7), which becomes the standard map [20] for $\delta = 0$. We instead investigate the modified standard map with δ in the first (area-contracting) term on the right hand side of (7a) set to zero, but with the small correction due to the last term $-u_k\delta$ retained:

$$I_{n+1} = I_n + K \sin\theta_n - u_k\delta. \qquad (7a')$$

The system is Hamiltonian and we can obtain the primary and secondary islands either numerically or analytically.

Figure 6 shows the iteration of (7') for $M = 100$, $\delta = 0.01$, $k = 7$ and 8. For $k = 7$, a period 3 island chain surrounds the primary island, and both are enclosed within a large KAM curve. For $k = 8$, a period 5 island chain closely surrounds the last KAM curve of the primary long island, and another period 3 island chain surrounds the period 5 chain. We further find that when the first (dissipative) term is retained in (7'), the fixed points at the island centers become sinks. Figure 7 shows the sinks for the Fermi map (3) with the same M and δ. We see that a period 1 and a period 3 sink coexist at $k = 7$, and that a period 2 and a period 5 sink coexist at $k = 8$. The patterns in Fig. 7 resemble those in Fig. 6, except for an inversion in polarity due to the minus sign in (8a). It is evident that (7') locally approximates (3). The period 2 sink in (3) arises as a bifurcation of the period 1 sink within the long island, due to the finite value of δ. [For $\delta = 0$, the period 1 fixed point in (7') is just within

the border of stability, whereas in (3) it is just outside the border, as described below.]

For the standard map, a primary fixed point is stable for stochasticity parameter $K < 4$. Therefore we expect to see sinks in the region $u \gtrsim u_s$ of the Fermi map (3) where

$$2\pi M/u_s^2 \approx 4. \tag{14}$$

Moreover, for small initial velocities, u is bounded from above by the stochastic barrier u_b corresponding to $2\pi M/u_b^2 = K_b \approx 1$. Therefore we expect to see trajectories starting with low velocities to be attracted to sinks in the region $u_b \lesssim u \lesssim u_s$, corresponding to:

$$\begin{cases} 3 \lesssim k \lesssim 4 & \text{for } M = 30, \\ 5 \lesssim k \lesssim 8 & \text{for } M = 100, \\ 7 \lesssim k \lesssim 14 & \text{for } M = 300. \end{cases} \tag{15}$$

For $M = 100$, $K \approx 4.02$ at the $k = 8$ fixed point at $\delta = 0$. A bifurcation accounts for the period 2 sink shown in Fig. 7 and in Table II. The same effect is found for $k = 15$ and 16 at $M = 300$.

In several cases shown in Table II, a few of the hundred initial conditions were attracted to a primary resonance having period two and three (fractional k). For period two, these resonances, $u_{n+2} = u_n$, $\psi_{n+2} = \psi_n \pmod{2\pi}$, are located near $u_k \approx 2M/k$, k odd, and are stable within some parts of region (ii). Similar properties hold for period three. We believe the effect of these higher period sinks can be included by considering the square, cube, etc. of the map (3).

We now determine the phase space area ΔA_k in the transiently chaotic region that is "eaten" by each primary island (including all its associated secondary island chains) during one iteration of (7). The standard map [(7) with $\delta = 0$] has a closed KAM barrier $I(\theta)$ with area $\bar{A}$ surrounding the central fixed point $(I, \theta) = (0, \pi)$. This barrier curve separates the outer chaotic region from the inner closed island orbits. For $\delta > 0$, $\bar{A}$ contracts by the factor $1 - \delta$. Thus $\Delta\bar{A} = \bar{A}\delta$. Transforming back to the (u, ψ) variables of the Fermi map (3), we obtain

$$\Delta A_k(u_k) = \bar{A}\delta/K. \tag{16}$$

$\bar{A}$ is a function of $K = u_b^2/u_k^2$ alone that can be found analytically [22,23] or numerically [11]. A good approximation for $1 < K < 6$ is $\bar{A} \approx 2\pi^2 K^{-1.3}$ for the standard map. Figure 8 shows the comparison of this approximation with the numerically determined [11] $\bar{A}$. But we have chosen to determine $\bar{A}$ numerically using (7'). In this way, the small correction in $\bar{A}$ due to the last term $-u_k\delta$ in (7a) is included. This numerically determined $\bar{A}$ is shown in Table III for various M and k (note $K = 2\pi M/u_k^2 = 2\pi k^2/M$).

Chirikov *et al.* [24] showed numerically that the decay rate into a sink varies directly as the stable area ΔA_k of the corresponding Hamiltonian ($\delta = 0$) map. For non-uniform f_Q, however, the decay rate should also be proportional to f_Q at the sink.

We can then estimate the decay rate $\bar{\alpha}$ for the transiently chaotic region as follows:

$$\bar{\alpha} = \sum_k \alpha_k, \tag{17a}$$

where

$$\alpha_k = f_Q(u_k)\Delta A_k \tag{17b}$$

and the sum is over all stable primary fixed points u_k in the region $u_s < u < u_b$. With f_Q known from (13), we can obtain the exponential decay rate $\bar{\alpha}$ from (17). The second entry in Table I gives $\bar{\alpha}$ thus obtained. The agreement with the numerically determined $\bar{\alpha}$ is generally quite good. The third entry in Table I is obtained similarly, except that $\gamma = 3$ is used instead of $\gamma = 2$. The agreement is not so good as for $\gamma = 2$ in general.

V. Distribution of Trajectories into Sinks

We have seen that all trajectories in the eleven cases having transient chaos are ultimately attracted to the stable fixed points of the map. The fraction of initial phase points that ultimately stick to each sink (including its secondary fixed points) can also be found analytically using (17b). Table IV shows the final numerical distribution g^n of 100 initial conditions into the various possible sinks for various M and δ. The corresponding distribution g^a_γ obtained analytically using (17b) with $\gamma = 2$ is also shown, with the sum of points attracted chosen to match that of the numerical sum. The ratios $R_k = g^a_2(k)/g^n(k)$ of analytical-to-numerical occupations for the sinks with various k's are shown in Fig. 9. We see that the agreement between numerical observation and analytical theory is good.

To compare the observations and the theory quantitatively, we use the mean square hyperbolic deviation [9] E^2 as the measure of resemblance between

the analytical and numerical distributions, where the numerical distribution is corrupted by the noise of Poisson counting statistics due to the finite number $L = 100$ of initial phase points chosen. For two distributions g^a (analytical) and g^n (numerical), each having L occupations in a domain that has been partitioned into K sinks, we write

$$E^2 = \frac{4}{L}\sum_{j=1}^{K}\left(\sqrt{g_j^a} - \sqrt{g_j^n}\right)^2, \tag{18}$$

where $g_j^a \geq 0$ and $g_j^n \geq 0$ are the number of occupations in sink j. For $M = 30$, 100, 300, we have $K = 2$, 4, 10 respectively. Introducing the mean occupation number $\mu = L/K$, E represents the (hyperbolic rms) number of standard deviations $\sqrt{\mu}$ by which g^a and g^n differ. Two distributions closely resemble each other if $E^2 \lesssim 1$. We see from Table IV that E^2 between g^n and g^a is generally less than or of the order E_R^2; i. e. the fit between the analytical theory and the numerical result, the latter corrupted by noise, is generally good. (Here E_R^2 is the square of the expected deviation [9] between a uniform distribution and a random distribution having Poisson statistics, both having the same μ and K as the numerical result.) However, the agreement is not so good for those cases where a significant primary sink is found near $u \lesssim u_b$, where f_Q obtained using $\gamma = 2$ deviates much from $\bar{f}$; an example is $M = 30$ and $\delta = 0.01$.

We repeat the calculation of E^2 using $\gamma = 3$ instead of 2 in (11); the result is also shown in Table IV. For $M = 30$ and $\delta = 0.01$, $\gamma = 3$ improves the agreement, as it gives a better fit f_Q to $\bar{f}$ near the sink with largest u. For $M = 100$ and $\delta = 0.001$, as well as for $M = 300$ and $\delta = 0.0003$, we see the same improvement for $\gamma = 3$ for the same reason. We expect a better estimate for

$\bar{D}$ in (11) to yield even closer agreement between the theory and the numerical results for $\bar{\alpha}$ and α_k as well as for the ratio of distributions into the various sinks.

In three cases for $M = 300$, period 2 sinks corresponding to $k = 15$ and 16 are observed. These sinks are bifurcated fixed points at $u < u_s$, and are therefore not included in the analytical results. This accounts for the relatively large E_γ^2 for each of these cases. We expect that including these bifurcated sinks in the analysis will further improve the theory.

VI. Conclusion

The transient chaos for a dissipatively perturbed area-preserving twist map has been studied analytically. The dissipative Fermi map has been used as as illustrative example. The quasistatic distribution f_Q is found by solving the appropriate Fokker–Planck equation for the map, with the diffusion coefficient D obtained from the modified standard map as a local approximation. The actual diffusion coefficient, and not its quasilinear approximation, must be used, with D vanishing when the stochasticity parameter decreases to $K \approx 1$. We find that for various M and δ, f_Q is a good approximation to the numerical result.

The rate α_k that the transient chaos is absorbed into an island sink is obtained from the product of f_Q mentioned above and the effective phase space area ΔA_k absorbed into the island sink per iteration. The island area A_k is obtained from the product of the dissipation coefficient δ and the area enclosed

by the corresponding KAM curve(s) in the area preserving ($\delta = 0$) map. We then obtain the mean lifetime of the transient chaos, as well as the distribution of initial trajectories into various sinks. We find that for various M and δ, the mean lifetime thus obtained compares well to the numerical result, and the distribution into the various sinks quantitatively resembles the numerical result.

We also observe from Table II that surrounding a primary sink at u_k, there are a number of secondary sinks of longer period than unity. For instance, Fig. 7 shows secondary sinks surrounding primary ones at $u_7 = 14.3$ and $u_8 = 12.5$. We have determined only the total fraction of initial trajectories absorbed by an island, but not the distribution among the primary and secondary sinks within the island. We believe that the latter distribution might be determined by applying the same theory to a separatrix map [2,11] obtained from a transformation [25] at the primary resonance u_k.

We note that the dynamics of dissipatively perturbed systems can generally be described in terms of dissipatively perturbed twist maps, to which the application of the above theory seems quite straightforward. We expect that the theory is applicable to a wide class of dissipatively perturbed near-integrable systems.

Acknowledgments

The support of the Office of Naval Research Contract N00014-84-K-0367 and the National Science Foundation Grant ECS-8104561 is gratefully acknowledged. We thank A. J. Lichtenberg for his comments on the manuscript.

References

[1] A. J. Lichtenberg and M. A. Lieberman, *Regular and Stochastic Motion*, (Springer, New York, 1982), Appendix A.

[2] Reference 1, Ch. 3.

[3] Reference 1, Ch. 7.

[4] R. H. G. Helleman, in *Fundamental Problems in Statistical Mechanics*, vol. **5**, E. G. D. Cohen, ed. (North-Holland, Amsterdam, 1980), p. 165.

[5] R. Shaw, *Z. Naturforsch.* **36A** (1981) 80.

[6] E. Ott, *Rev. Mod. Phys.* **53** (1981) 655.

[7] M. Hénon, *Commun. Math. Phys.* **50** (1976) 69.

[8] B. A. Huberman, private communication (1982).

[9] K. Y. Tsang and M. A. Lieberman, *Physica* **11D** (1984) 147.

[10] K. Y. Tsang and M. A. Lieberman, *Phys. Lett.* **103A** (1984) 175.

[11] B. V. Chirikov, *Phys. Reports* **52** (1979) 263.

[12] G. M. Zaslavskii, *Phys. Lett.* **69A** (1978) 145.

[13] E. Fermi, *Phys. Rev.* **75** (1949) 1169.

[14] M. A. Lieberman and A. J. Lichtenberg, *Phys. Rev.* **A5** (1972) 1852.

[15] G. M. Zaslavskii and B. V. Chirikov, *Soviet Physics Doklady* **9** (1965) 989.

[16] A. Brahic, *Astr. and Astrophys.* **12** (1971) 98.

[17] A. J. Lichtenberg, M. A. Lieberman and R. H. Cohen, *Physica* **1D** (1980) 291.

[18] Reference 1, pp. 436–442.

[19] Reference 1, sec. 5.4.

[20] Reference 1, sec. 4.1.

[21] A. B. Rechester, M. N. Rosenbluth and R. B. White, *Phys. Rev.* **A23** (1981) 2664.

[22] N. M. Murray, M. A. Lieberman and A. J. Lichtenberg, "Corrections to Quasilinear Diffusion in Area-Preserving Maps," *Electronics Research Laboratory Report UCB/ERL* **M84/102**, University of California, Berkeley; to appear in *Phys. Rev. A* (1985).

[23] A. J. Lichtenberg, *Nucl. Fusion* **24** (1984) 1277.

[24] B. V. Chirkov and F. M. Izraelev, *Physica* **2D** (1981) 30.

[25] Reference 1, sec. 2.4 and 4.3.

Tables

Table I. Decay rates $\bar{\alpha}$ (in units of 10^{-5}), for various M and δ. The first entry is determined by numerical iteration of the Fermi map; The second and the third entries are determined analytically by the method introduced in Sec. III using $\gamma = 2$ and 3 respectively.

Table II. Numbers of trajectories entering sinks of period p and at $u \approx M/k$, for 100 initial conditions chosen randomly at small u. Number of iterations $N = 50\,000$ except for $M = 300$ or for $\delta = 0.0003$, where $N = 200\,000$ instead.

Table III. Area $\bar{A}$ of regular regions for the modified standard map determined numerically (in units of $4\pi^2$), with $K = 2\pi k^2/M$.

Table IV. Final distributions g^n (numerical) and g^a_γ (analytical, $\gamma = 2$ and 3), into sinks corresponding to different k's for 100 initial conditions, the expected deviation from Poisson counting statistics E^2_R, and the deviations E^2_2 and E^2_3 between the numerical and the two analytical results; (a) $M = 30$; (b) $M = 100$; and (c) $M = 300$.

Figure Captions

Fig. 1. Phase space y–x for the periodic Hénon map with $a = 1.4$ and $b = 0.9$. (a) Numerically obtained from one initial condition ($\times$) with 10 000 iterations; (b–d) analytically obtained second, third, and fifth order results using uniform zeroth order distribution.

Fig. 2. Phase space y–x for the periodic Hénon map with $a = 1.4$ and $b = 0.9$ obtained numerically for 100 000 iterations; (a) and (b) are two different initial conditions ($\times$). Both are attracted to a period six attractor (dots).

Fig. 3. Number of unattracted trajectories N_u versus number of iterations n for the dissipative Fermi map with various δ's. (a) $M = 30$; (b) $M = 100$; (c) $M = 300$.

Fig. 4. Cumulative, phase-averaged distributions $\bar{f}$ versus u, after 5×10^4 iterations of 100 randomly chosen initial conditions, for various M and δ. The solid curve shows the numerical result; the dashed and dotted curves show the quasistatic theory f_Q with $\gamma = 2$ and 3 respectively.

Fig. 5. Diffusion coefficient $\bar{D}$ versus stochasticity parameter K for the standard map. The solid curve shows the numerical result [22]; dashed curve shows the parabolic approximation used to obtain f_Q.

Fig. 6. Features of the modified standard map obtained numerically with $M = 100$ and $\delta = 0.01$. The stochasticity parameter K corresponds to (a) $k = 7$; (b) $k = 8$.

Fig. 7. Sinks for the Fermi map obtained numerically with $M = 100$ and $\delta = 0.01$. Note the correspondence to Fig. 6. (There is an inversion in polarity since $I \approx -\Delta u$, $\psi = \theta$)

Fig. 8. Area of regular regions $\bar{A}(K)$ for standard map versus the stochasticity parameter K. The solid curve shows the numerical result [11]; the dashed curve shows an analytical fit to the numerical result: $\bar{A} = 2\pi^2 K^{-1.3}$.

Fig. 9. The ratio R_k of the analytically-to-numerically determined fractions of trajectories atractted to the various sinks, for all the cases given in Table I.

TABLE I

M/δ	.0003	.001	.003	.01
30	2.0/2.5/2.4	2.7/6.6/5.5	7.4/12.0/7.8	7.7/8.6/5.1
100	1.2/2.0/1.6	2.0/3.6/2.4	2.9/2.6/1.7	1.1/.29/.12
300	1.1/1.1/.70	1.1/.90/.53	.40/.16/.07	

TABLE II

M = 30

p \ k	$2\frac{1}{2}$	$2\frac{2}{3}$	3	4
1	0	0	47	13
2	8	0	0	0
3	0	2	0	6
5	0	0	4	0
7	0	0	0	1
9	0	0	4	0

$\delta = 10^{-3}$

p \ k	3	4_r
1	55	9
3	0	7
5	6	0

$\delta = 3\times10^{-3}$

p \ k	3	4
1	59	13
3	0	25
5	1	0

$\delta = 10^{-2}$

p \ k	3	4
1	1	30
3	0	65
5	2	0

M = 100

p \ k	5	$5\frac{1}{2}$	6	7	8
1	20	0	13	8	0
2	0	6	0	0	5
3	0	0	0	9	0
4	0	0	9	0	0
5	5	0	1	0	1
6	2	1	0	0	0
8	0	0	0	0	1

$\delta = 10^{-3}$

p \ k	5	$5\frac{1}{2}$	6	7	8
1	0	0	11	1	0
2	0	1	0	0	5
3	0	0	0	21	1
4	0	0	17	0	0
5	1	0	0	0	3

$\delta = 3\times10^{-3}$

p \ k	6	7	8
1	5	8	0
2	0	0	14
3	0	24	0
4	12	0	0
5	0	0	12

$\delta = 10^{-2}$

p \ k	7	8
1	2	0
2	0	26
3	6	0
5	0	10

M = 300

p \ k	9	$9\frac{1}{2}$	10	11	12	13	14	15
1	7	0	9	11	2	10	0	0
2	0	1	0	0	0	0	7	1
3	0	0	0	0	6	6	0	0
4	0	0	16	0	0	0	0	0
5	2	0	0	0	0	0	1	0

$\delta = 10^{-3}$

p \ k	10	11	12	13	14	15	16
1	6	7	5	14	0	0	0
2	0	0	0	0	16	3	1
3	0	0	17	3	0	0	0
4	4	0	0	0	0	0	0
5	0	0	0	0	5	0	0
7	0	0	2	0	4	0	0
8	0	0	0	0	1	0	0
9	0	0	0	0	1	0	0

$\delta = 3\times10^{-3}$

p \ k	11	12	13	14	15
1	1	0	6	0	0
2	0	0	0	11	4
3	0	8	6	0	0
5	0	0	0	8	0
7	0	0	0	5	0

TABLE III

M	k	$\delta = 0.0003$	$\delta = 0.001$	$\delta = 0.003$	$\delta = 0.01$
30	3	.27	.23	.22	.18
	4	.12	.11	.105	.10
100	5	.26	.22	.23	.25
	6	.20	.18	.11	.25
	7	.12	.12	.12	.10
	8	.09	.095	.065	.05
300	8	.30	-	-	-
	9	.22	.24	-	-
	10	.22	.24	.20	-
	11	.11	.10	.09	-
	12	.11	.11	.11	-
	13	.10	.105	.10	-
	14	.07	.06	.07	-

M = 30

TABLE IV(a)

δ	k	g^n	E_R^2	g_2^a	E_2^2	g_3^a	E_3^2
0.0003 ($N=2\times10^5$)	3*	65	.024	66.9	.003	66.0	.001
	4	20		18.1		19.0	
0.001	3	61	.026	57.0	.015	53.8	.046
	4	16		20.0		23.2	
0.003	3	60	.020	61.4	.001	46.5	.077
	4	38		36.6		51.5	
0.01	3	3	.020	18.0	.283	2.7	.000
	4	95		80.0		95.3	

*including $k = 2\frac{1}{2}$ and $2\frac{2}{3}$

TABLE IV(b)

M=100

δ	k	g^n	E_R^2	g_2^a	E_2^2	g_3^a	E_3^2
0.0003 ($N=2\times10^5$)	5*	34	.049	34.1	.020	24.8	.073
	6	23		26.1		30.1	
	7	17		12.9		16.1	
	8	7		7.9		10.0	
0.001	5*	2	.067	11.4	.329	2.5	.096
	6	28		21.6		21.6	
	7	22		15.6		20.1	
	8	9		11.4		15.9	
0.003	5	0	.053	1.1	.073	0.0	.158
	6	17		13.5		6.5	
	7	32		34.9		35.7	
	8	26		25.5		32.8	
0.01	5	0	.091	0.0	.134	0.0	.008
	6	0		0.8		0.0	
	7	8		12.3		6.8	
	8	36		30.9		37.1	

*including $k = 5\frac{1}{2}$

TABLE IV(c)

M = 300 ($N=2\times10^5$)

δ	k	g^n	E_R^2	g_2^a	E_2^2	g_3^a	E_3^2
0.0003	8	0	.112	4.5	.359	0.1	.159
	9*	10		14.3		6.8	
	10	25		21.0		19.9	
	11	11		11.7		14.0	
	12	8		11.7		15.5	
	13	16		10.2		14.2	
	14	8		6.6		9.6	
	15	1		0		0	
	16	0		0		0	
0.001	8	0	.110	0.0	.457	0.0	.365
	9	0		2.1		0.1	
	10	10		12.3		4.3	
	11	7		11.4		8.6	
	12	24		18.9		20.1	
	13	17		22.6		28.6	
	14	27		14.6		20.3	
	15	3		0		0	
	16	1		0		0	
0.003	8	0	.184	0.0	.382	0.0	.451
	9	0		0.0		0.0	
	10	0		0.2		0.0	
	11	1		1.2		0.2	
	12	8		7.0		3.9	
	13	12		17.2		15.9	
	14	24		23.4		28.9	
	15	4		0		0	
	16	0		0		0	

*including k = $9\frac{1}{2}$

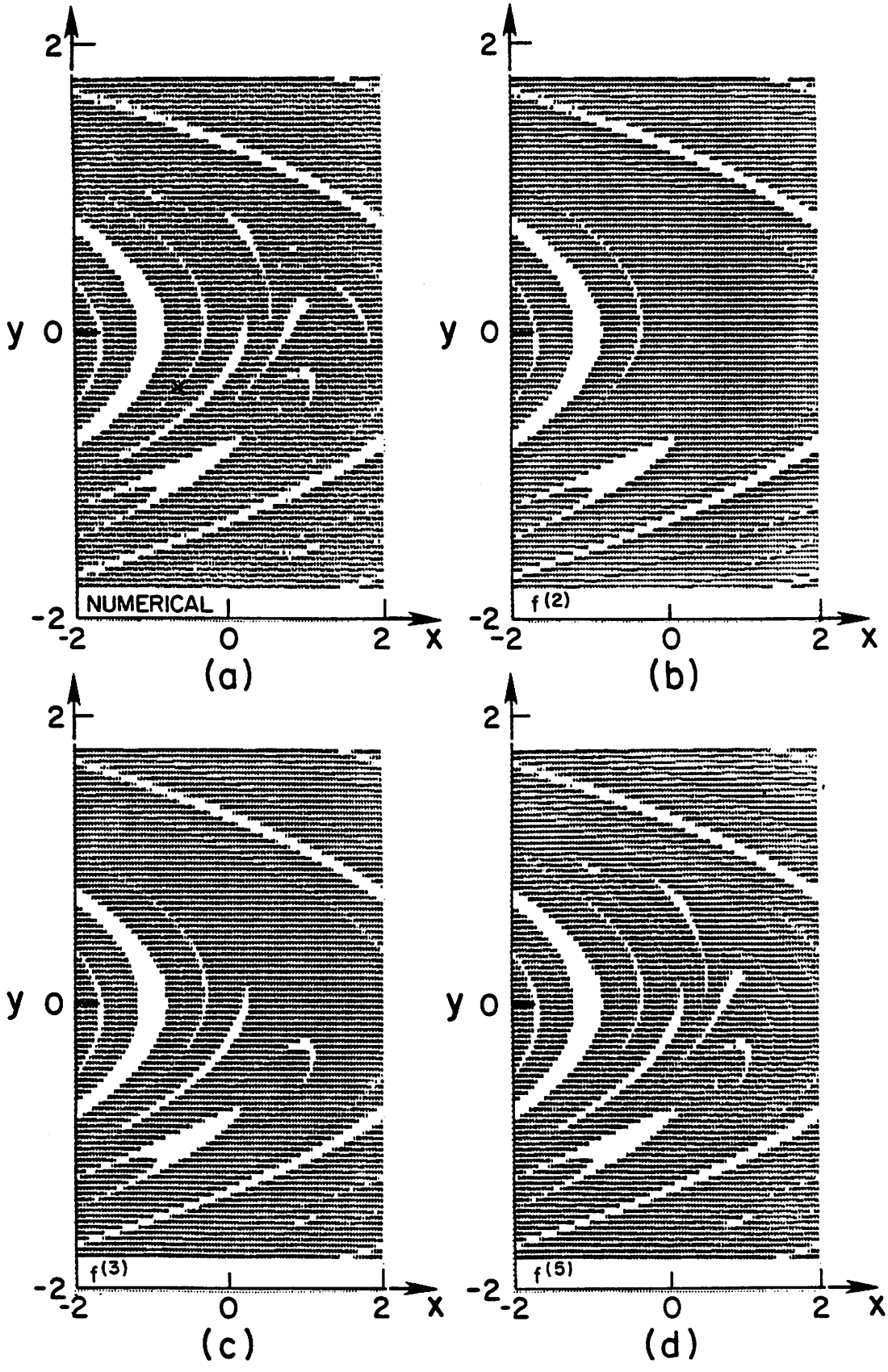
2
y 0
-2
NUMERICAL
-2
0
2
x
(a)
2
y 0
-2
f(2)
-2
0
2
x
(b)
2
y 0
-2
f(3)
-2
0
2
x
(c)
2
y 0
-2
f(5)
-2
0
2
x
(d)

Fig. 1

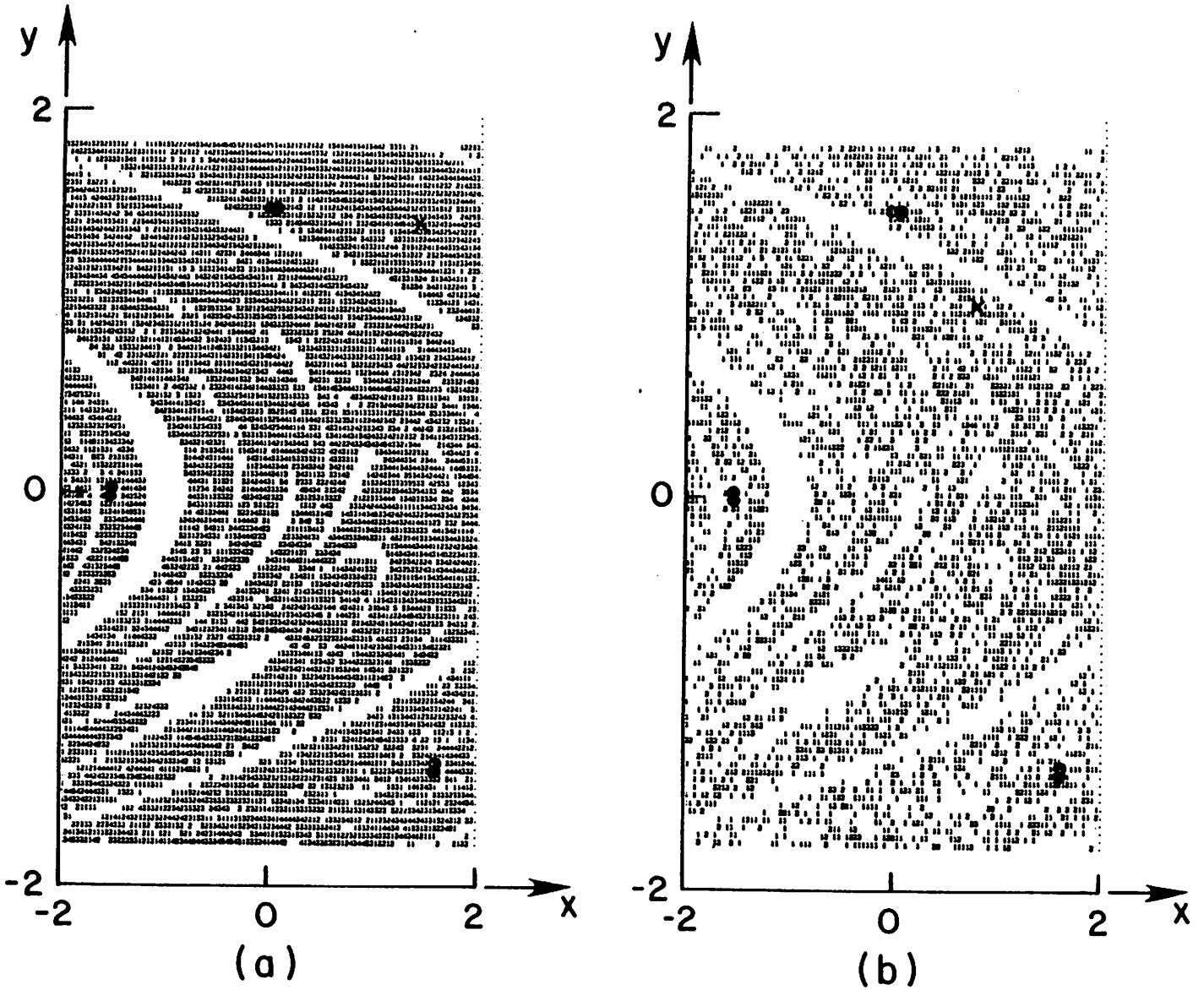

Fig. 2

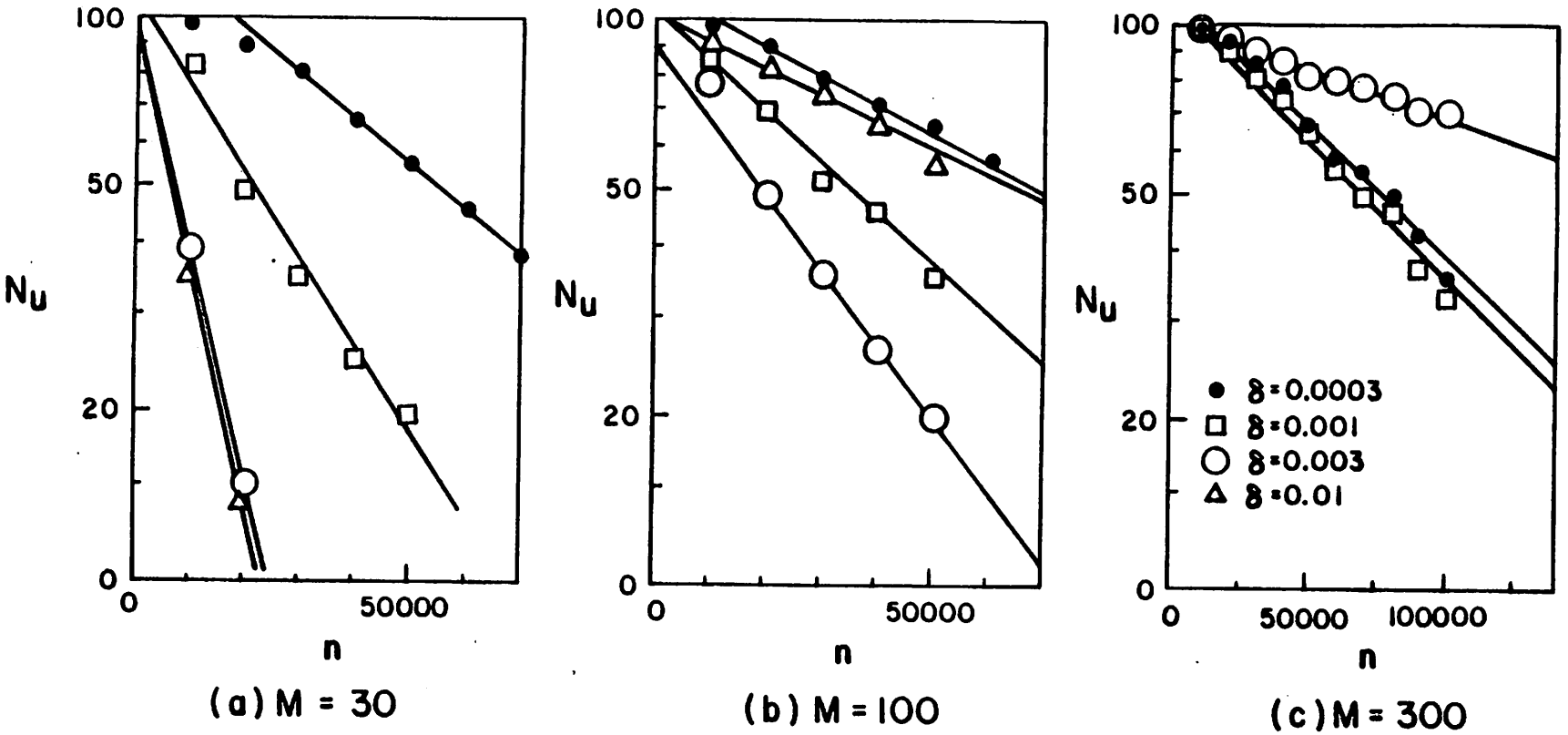
100
50
20
0
0
50000
100000
N_u
n
δ=0.0003
δ=0.001
δ=0.003
δ=0.01
(a) M = 30
(b) M = 100
(c) M = 300

Fig. 3

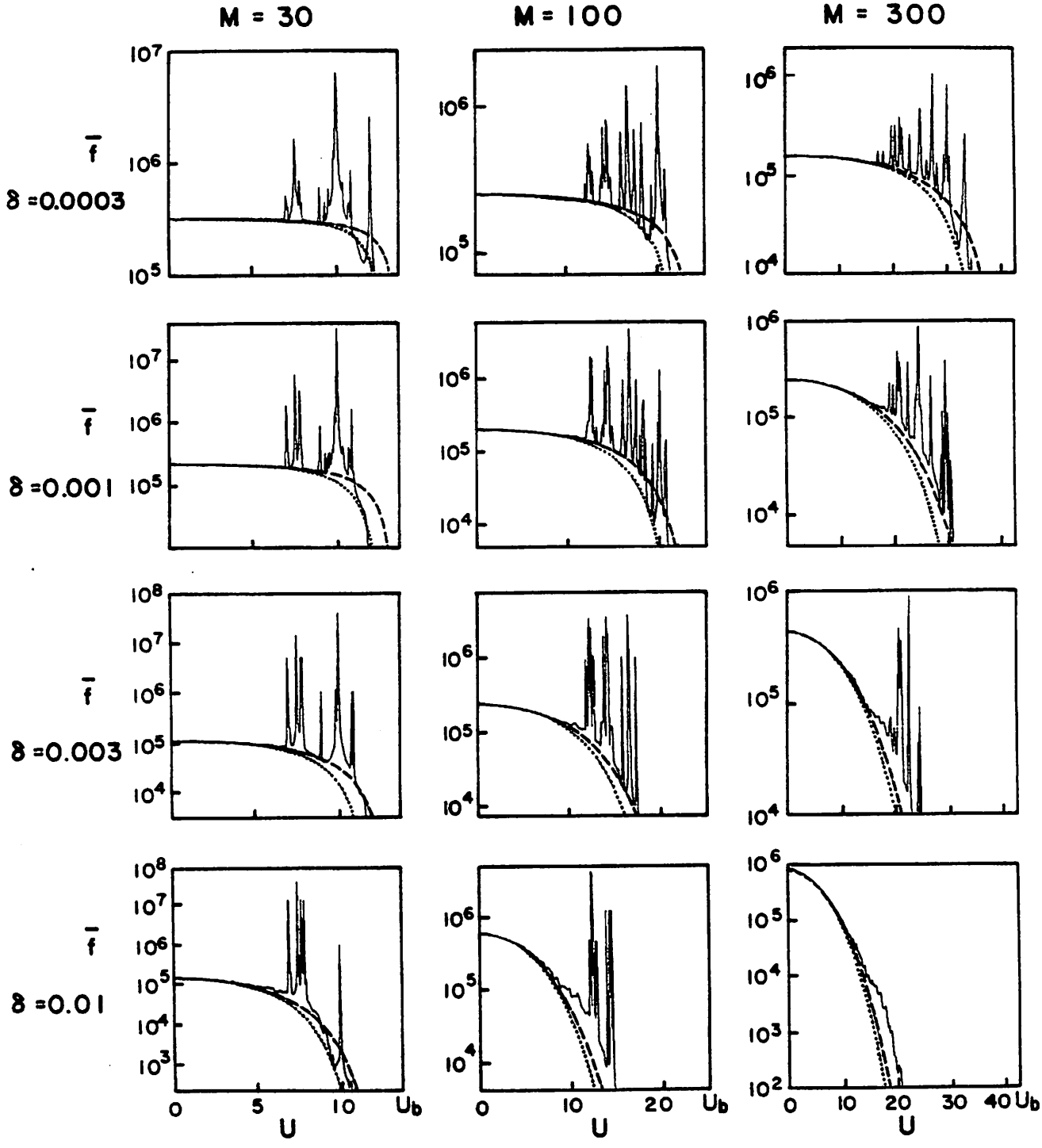

Fig. 4

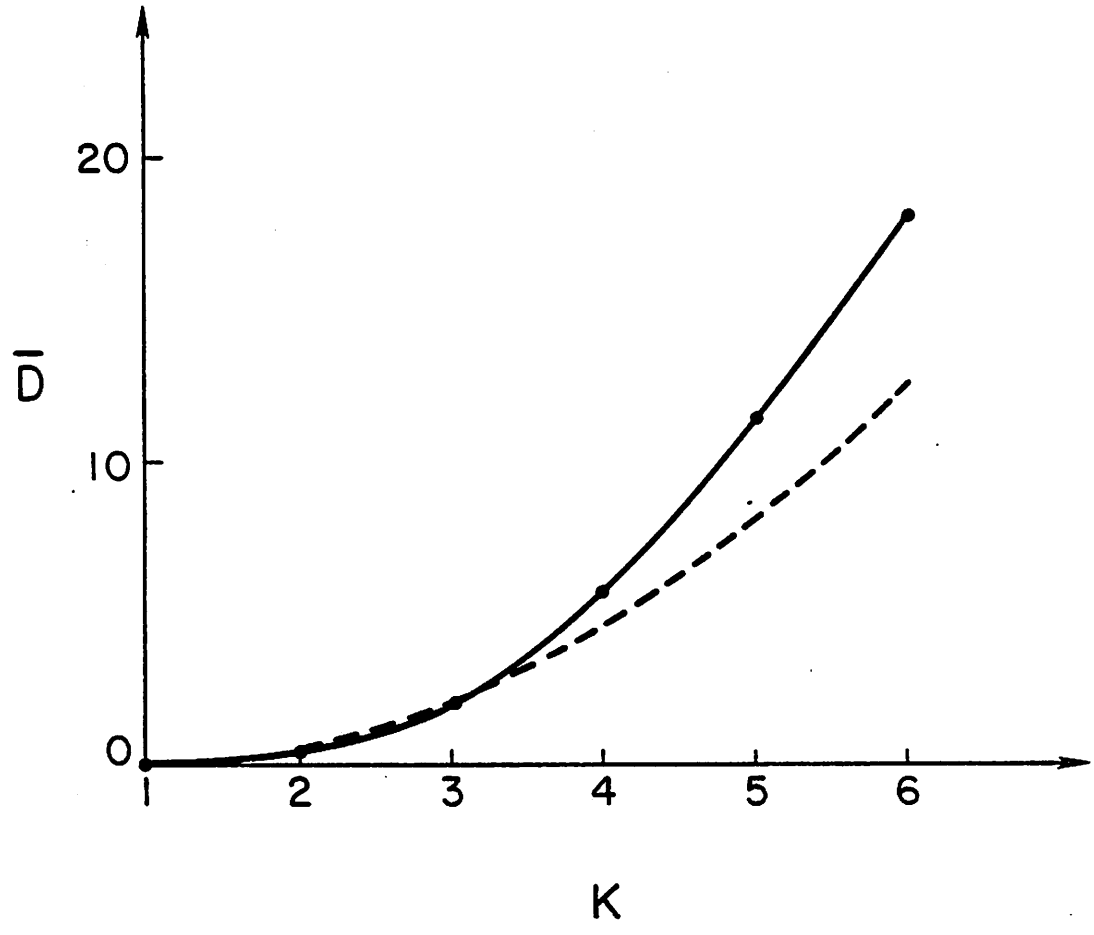

Fig. 5

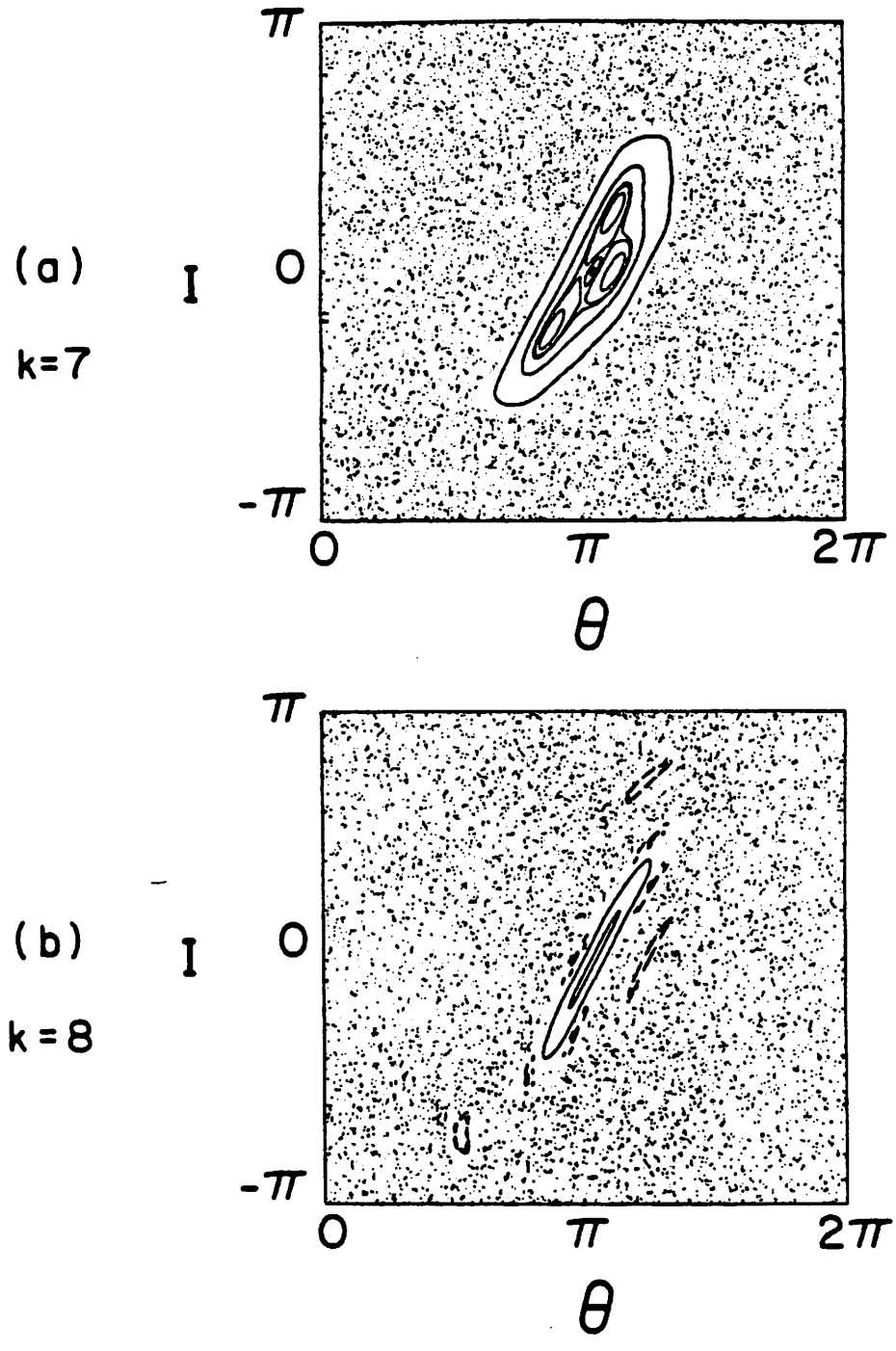

Fig. 6

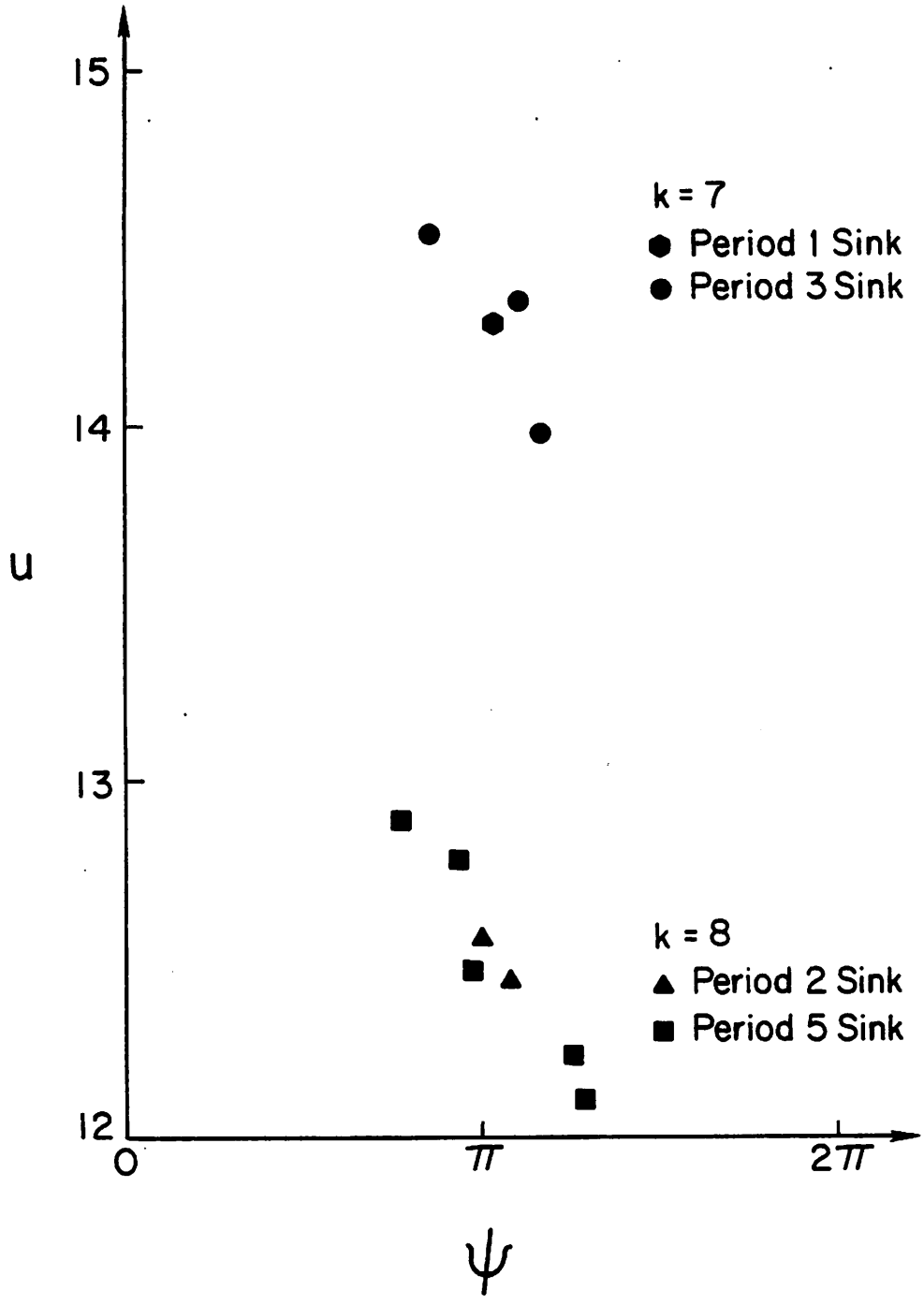
15
14
13
12
u
0
π
2π
ψ
k = 7
Period 1 Sink
Period 3 Sink
k = 8
Period 2 Sink
Period 5 Sink

Fig. 7

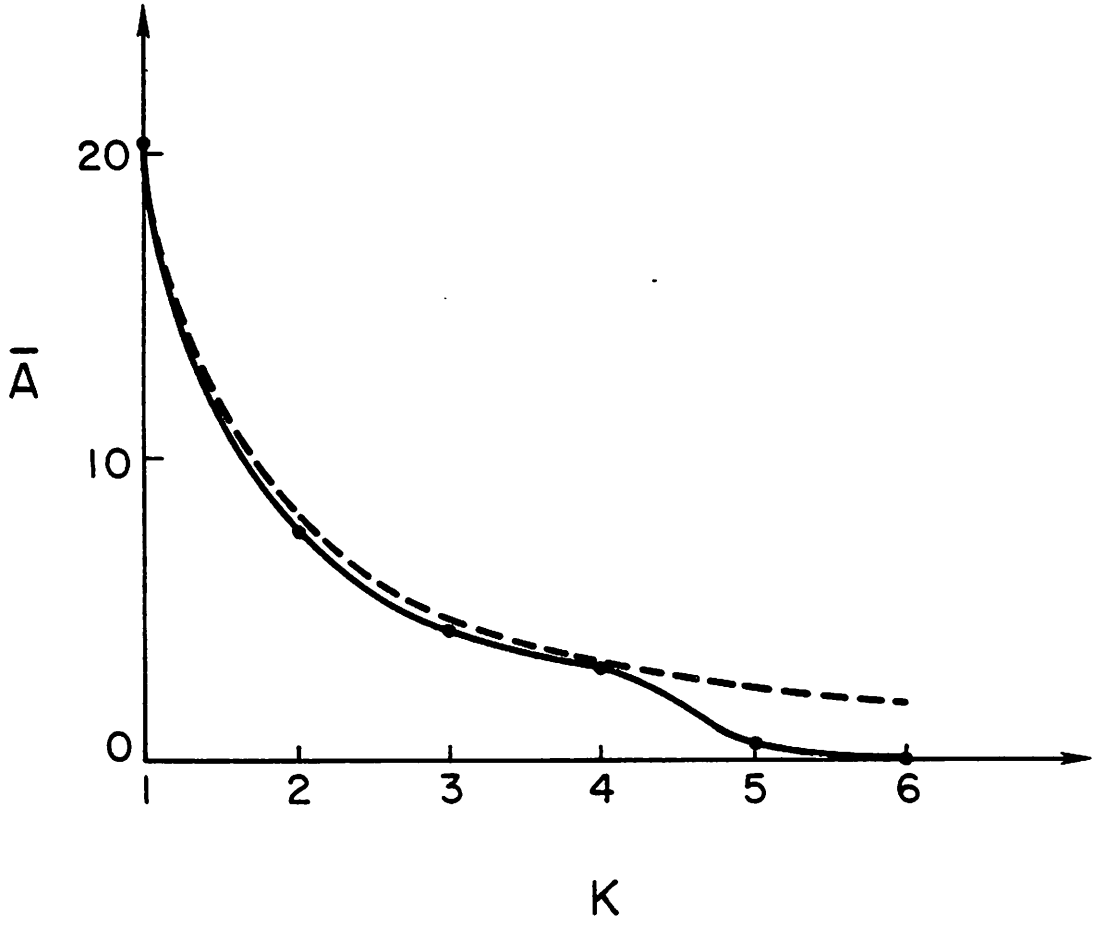

Fig. 8

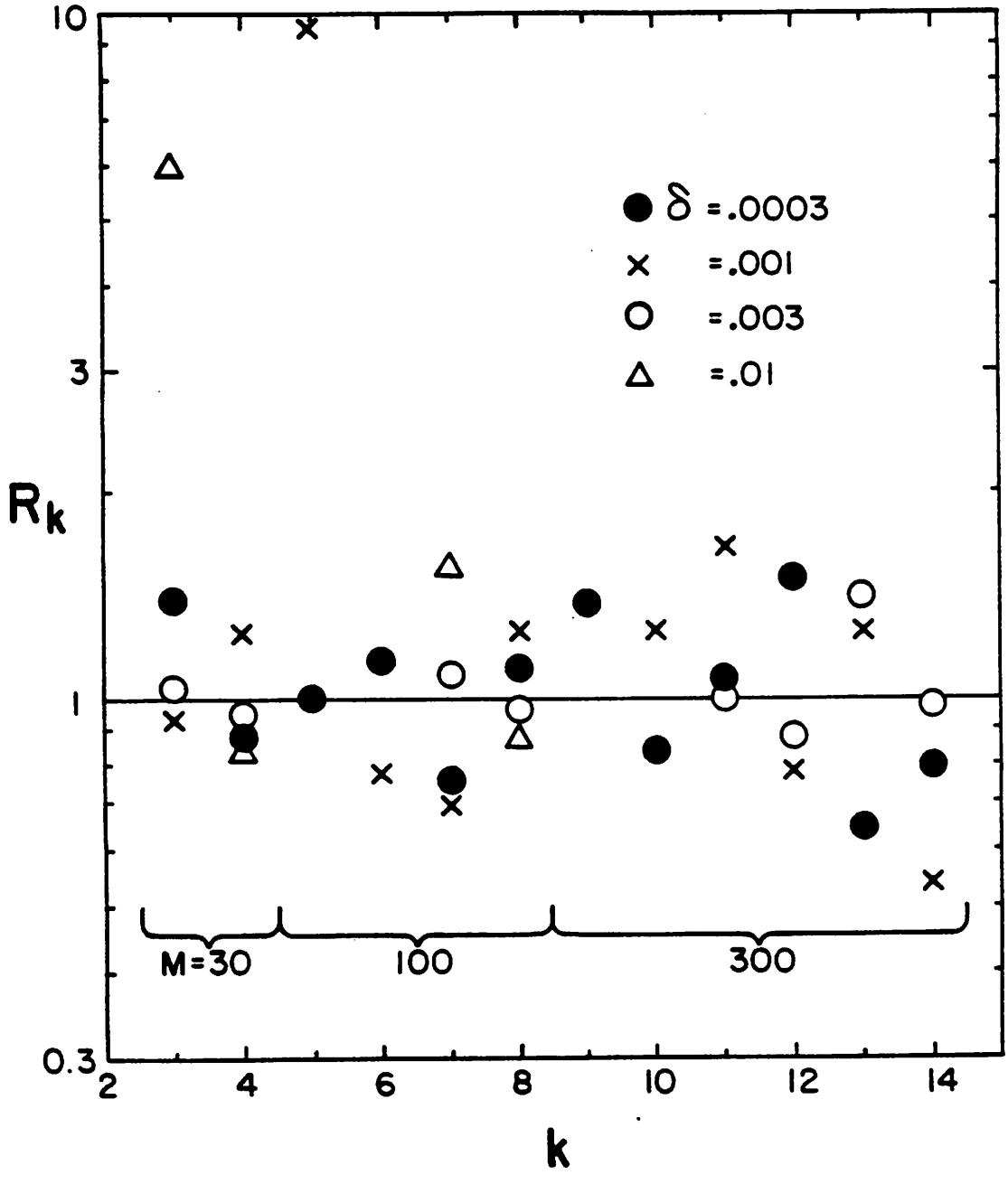

Fig. 9